New Constraints on the free-streaming of warm dark matter from intermediate and small scale Lyman-α forest data

Vid Iršič[1,2,3],* Matteo Viel[4,5,6],† Martin G. Haehnelt [7], James S. Bolton [8], Stefano Cristiani[5,6],
George D. Becker[7,9], Valentina D'Odorico[5], Guido Cupani[5], Tae-Sun Kim[5], Trystyn A. M. Berg[10],
Sebastian López[11], Sara Ellison[10], Lise Christensen[12], Kelly D. Denny[13], and Gábor Worseck[14]

[1]*University of Washington, Department of Astronomy,*
3910 15th Ave NE, WA 98195-1580 Seattle, USA
[2]*Institute for Advanced Study,*
1 Einstein Drive, NJ 08540 Princeton, USA
[3]*The Abdus Salam International Centre for Theoretical Physics,*
Strada Costiera 11, I-34151 Trieste, Italy
[4] *SISSA-International School for Advanced Studies,*
Via Bonomea 265, 34136 Trieste, Italy
[5]*INAF - Osservatorio Astronomico di Trieste,*
Via G. B. Tiepolo 11, I-34143 Trieste, Italy
[6]*INFN - National Institute for Nuclear Physics,*
via Valerio 2, I-34127 Trieste, Italy
[7] *Institute of Astronomy and Kavli Institute of Cosmology,*
Madingley Road, Cambridge CB3 0HA, UK
[8] *School of Physics and Astronomy,*
University of Nottingham, University Park,
Nottingham, NG7 2RD, UK
[9]*Space Telescope Science Institute,*
3700 San Martin Drive, Baltimore, MD 21218, USA
[10]*Department of Physics and Astronomy,*
University of Victoria, Victoria, BC V8P 1A1, Canada
[11]*Departamento de Astronomía,*
Universidad de Chile, Casilla 36-D, Santiago, Chile
[12]*Dark Cosmology Centre, Niels Bohr Institute,*
University of Copenhagen, Juliane Maries Vej 30,
DK-2100 Copenhagen, Denmark
[13]*Department of Astronomy,*
The Ohio State University, 140 West 18th Avenue,
Columbus, OH 43210, USA
[14]*Max-Planck-Institut für Astronomie,*
Königstuhl 17, D-69117 Heidelberg, Germany

We present new measurements of the free-streaming of warm dark matter (WDM) from Lyman-α flux-power spectra. We use data from the medium resolution, intermediate redshift XQ-100 sample observed with the X-shooter spectrograph ($z = 3-4.2$) and the high-resolution, high-redshift sample used in Viel et al. (2013) obtained with the HIRES/MIKE spectrographs ($z = 4.2 - 5.4$). Based on further improved modelling of the dependence of the Lyman-α flux-power spectrum on the free-streaming of dark matter, cosmological parameters, as well as the thermal history of the intergalactic medium (IGM) with hydrodynamical simulations, we obtain the following limits, expressed as the equivalent mass of thermal relic WDM particles. The XQ-100 flux power spectrum alone gives a lower limit of 1.4 keV, the re-analysis of the HIRES/MIKE sample gives 4.1 keV while the combined analysis gives our best and significantly strengthened lower limit of 5.3 keV (all 2σ C.L.). The further improvement in the joint analysis is partly due to the fact that the two data sets have different degeneracies between astrophysical and cosmological parameters that are broken when the data sets are combined, and more importantly on chosen priors on the thermal evolution. These results all assume that the temperature evolution of the IGM can be modelled as a power law in redshift. Allowing for a non-smooth evolution of the temperature of the IGM with sudden temperature changes of up to 5000K reduces the lower limit for the combined analysis to 3.5 keV. A WDM with smaller thermal relic masses would require, however, a sudden temperature jump of 5000 K or more in the narrow redshift interval $z = 4.6 - 4.8$, in disagreement with observations of the thermal history based on high-resolution resolution Lyman-α forest data and expectations for photo-heating and cooling in the low density IGM at these redshifts.

PACS numbers:

---

*E-mail: irsic@uw.edu (VI)

†E-mail: viel@sissa.it (MV)

I. INTRODUCTION

The intergalactic medium (IGM) and its main observable manifestation, the Lyman-α forest (see [1]), have been used as unique tools to address key cosmological issues: the free-streaming of dark matter and in particular departures from cold dark matter, generally labelled as warm dark matter (WDM) [2–8]; measuring the linear power spectrum at small scales [9–14]; probing the effect of the free-streaming and thus the masses of neutrinos [14, 15], and placing (high-redshift) geometrical constraints on our Universe from Baryonic Acoustic Oscillations measurements [16, 17].

At present, constraints on the matter power spectrum are either derived from moderate size samples with tens of high-resolution, high signal-to-noise spectra (VLT, HIRES/KECK, [7, 9, 12]) or large samples with thousands of low-resolution, low signal-to-noise spectra (SDSS-II, SDSS-III/BOSS, [13, 18, 19]). The XQ-100 [20] sample bridges the gap between these two regimes with its homogeneous set of intermediate resolution and intermediate signal-to-noise QSO absorption spectra, with the additional benefit that the flux power spectrum inferred from medium resolution QSO absorption spectra is subject to quite different systematic and statistical uncertainties. Here, we will provide constraints on the free-streaming length of dark matter from modelling the XQ-100 flux-power spectrum as well as from a combined analysis with new modelling of the HIRES/MIKE flux power spectrum presented in [7]. These two data sets have a small redshift overlap and it can be expected that a combined analysis will further break degeneracies with remaining uncertainties in the parameters describing the thermal evolution of the IGM, the evolution of the mean flux and cosmological parameters. Pushing the constraints on the free-streaming length of dark matter as far as possible is very relevant for the wider astrophysics community given that considerable tensions with the Cold Dark Matter (CDM) model on small scales continue to persist for a range of astrophysical observations, especially with regard to the dynamical properties of Milky Way satellites (see e.g [21]). From a particle physics point of view, small scale modifications of the cold dark matter power spectrum can *e.g.* arise from the free-streaming of sterile neutrinos [22–24] or ultralight bosons [25], alternatives to the more generic thermal relics on which we concentrate our modelling here [26]. For the purpose of our analysis here the different DM candidates differ in the exact shape of the suppression of the small scale power spectrum they cause due to free-streaming. However, apart from changing the nature of the DM several studies have shown that baryonic physics could help in alleviating or even solving the small scale tensions [27, 28].

In Section II we briefly describe the data sets used; Section III presents the hydrodynamical simulations grid; the method is briefly outlined in Section IV while Section V contains all the new results (with an Appendix focusing on degeneracies between the various parameters). We conclude with a summary in Section VI.

II. DATA SETS

We make use of two different and complementary data sets: the XQ-100 and HIRES/MIKE samples. XQ-100 consists of 100 medium resolution and signal-to-noise QSO spectra obtained as part of the XQ-100 survey with emission redshifts $3.5 < z < 4.5$ [20]. A detailed description of the data and the 1D flux power spectrum measurements is presented in [29]. The resolution of the XQ-100 spectra is $30-50 \mathrm{km\,s}^{-1}$ (FWHM) depending on wavelength and the pixel size used for calculating the flux power spectrum for the two spectral arms is 20 (UVB) and 11 $\mathrm{km\,s}^{-1}$ (VIS), respectively (see [29] for details).

The spectral resolution sets the smallest scales probed by the data. The flux power spectrum extraction has been extensively modeled with mock data sets built from hydrodynamic simulations which allows an accurate estimation of statistical and systematic uncertainties of the flux power at $z = 3, 3.2, 3.4, 3.6, 3.8, 4, 4.2$ for 19 bins in $k-$space in the range 0.003–$0.057\,\mathrm{s\,km}^{-1}$. In [29] the covariance matrix was multiplied with a constant factor 1.1, to correct for the underestimation of variance through the bootstrap method. We use the same correction factor here unless otherwise noted. We further assume that the cross-correlations between different redshift bins is zero. A total of 133 (k, z) points are thus used in our modelling of the XQ-100 flux power spectrum.

We also combine the new data with measurements of the power spectrum used in [7], measured at higher redshift $z = 4.2, 4.6, 5.0, 5.4$, for 10 $k-$bins in the range 0.001–$0.08\,\mathrm{s\,km}^{-1}$. The QSO absorption spectra of this sample have been obtained with the HIRES/KECK and the MIKE/Magellan spectrographs, with resolution 6.7 $\mathrm{km\,s}^{-1}$ and 13.6 $\mathrm{km\,s}^{-1}$, respectively. Following [7] a conservative cut is imposed on the MIKE and HIRES data, such that wavenumbers with $k < 0.005\,\mathrm{s\,km}^{-1}$ are removed, due to possible systematic uncertainties on the large scales of those measurements that used only a small number of QSO sightlines. Moreover, we also do not consider the highest redshift bin for the MIKE data, where the flux power spectrum measurements have large error bars. The analysis in [7] used a correction factor of 1.5 for the nominal error estimates of the flux power spectrum. We use the same value in our analysis here, unless otherwise stated. Ref. [7] further checked the error estimates using a sample of mock absorption spectra. This suggested that the two error bars in the MIKE and HIRES data sets with $\sigma_F/P_F < 0.075$ should be set to 0.075, which we also do in our analysis here (see [7] for more details). We further regularize the covariance matrix of the HIRES/MIKE data following the procedure of [7]. A total of 49 (k, z) points is used in the HIRES/MIKE

III. SIMULATIONS

Our analysis of the flux power spectrum is based on a set of hydrodynamical simulations that is significantly extended compared to that used in [7]. The hydrodynamical simulations were performed with the GADGET-3 code, which is a modified version of the publicly available GADGET-2 code [30]. A simplified star formation criterion is applied for which gas particles above an overdensity 1000 and temperature below T$= 10^5$ K are converted into stars (e.g. [31]). The reference model simulation has a box length of $20/h$ comoving Mpc with 2×768^3 gas and (cold) dark matter particles (with gravitational softening $1.04/h$ comoving kpc) in a flat ΛCDM universe with cosmological parameters $\Omega_{\mathrm{m}} = 0.301$, $\Omega_{\mathrm{b}} = 0.0457$, $n_{\mathrm{s}} = 0.961$, $H_0 = 70.2$ km s^{-1} Mpc^{-1} and $\sigma_8 = 0.829$ in agreement with [32]. Three different WDM models with masses $m_{\mathrm{WDM}} = 2, 3, 4$ keV have also been simulated. Initial conditions were implemented using the same approach as [3]. We explore the thermal history of the Lyman-α forest by modifying the photo-heating rates in the simulations as in [33]. The low density IGM ($\Delta = 1 + \delta < 10$) is well described by a power-law temperature-density relation, $T = T_0 \Delta^{\gamma - 1}$. We consider a range of values for the temperature at mean density T_0 and the slope of the $T - \rho$ relation, γ, based on the previous analysis of the Lyman-α forest and recent observations [34]. These consist of a set of three different temperatures at mean density, $T_0(z = 3.6) = 7200, 11000, 14800$ K, which evolve with redshift, as well as a set of three values of the slope of the $T - \rho$ relation: $\gamma(z = 3.6) = 1.0, 1.3, 1.5$. These 9 thermal history models have been simulated for the reference ΛCDM case; additionally all three different temperature models have been simulated for all three WDM models as well. The reference thermal history assumes $(T_0(z = 3.6), \gamma(z = 3.6)) = (11000 \text{ K}, 1.5)$.

Instead of using the standard cosmological parameters of σ_8, the slope of the initial power spectrum n_{s} and Ω_{m} as in [7], we exploit the fact that these three parameters are tightly connected in ΛCDM (and ΛWDM) models and impact on the flux power spectrum only in terms of the amplitude and the (effective) slope of the *matter* power spectrum *at scales that are probed by the Lyman-α forest*. We therefore use instead only two parameters describing cosmology, σ_8 and $n_{\mathrm{eff}} = d \ln P_{\mathrm{m}}(k)/d \ln k$, evaluated at $k = 0.005$ s km^{-1}, similarly to what was done in [13]. Five different values are considered for both $\sigma_8 = 0.754, 0.804, 0.829, 0.854, 0.904$, and $n_{\mathrm{eff}} = -2.3474, -2.3274, -2.3074, -2.2874, -2.2674$. The reference model has $(\sigma_8, n_{\mathrm{eff}}, n_{\mathrm{s}}) = (0.829, -2.3074, 0.961)$. Other cosmological parameters are kept fixed at the Planck best fit values. In practice, the change in n_{eff} is implemented with small changes of n_{s}.

We also vary the redshift of reionization z_{rei} which is chosen to be $z_{\mathrm{rei}} = 9$ for the reference model as well as $z_{\mathrm{rei}} = 7, 15$ for two additional models. The $z_{\mathrm{rei}} = 7$ model has also been simulated for all 3 values of the WDM thermal relic mass, since the redshift of reionization has an impact on the Jeans smoothing scale and could affect the cutoff scale of the flux power spectrum. We note here, however, that the effect is large enough for the degeneracy between free-streaming and Jeans smoothing to be broken (although see [35] in the context of CDM models) and that the data are not constraining this parameter well (see B for details).

The final parameter we explored characterizes the possible effect of ultraviolet (UV) background fluctuations. A model has been chosen where the spatial fluctuations of the meta-galactic UV background are dominated by rare QSOs, which has a strong scale dependent effect on the flux power spectrum particularly at high redshift and at large scales. The model of UV fluctuations used here is an update of the model presented in [7] (see appendix there). The updated model uses the more recent mean free path measurements of [36] and parameterizes the effect of UV fluctuations on the flux power spectrum as f_{UV} – defined as the fraction of the volume averaged hydrogen photo-ionisation rate that arises from a fluctuating QSO component. The remaining fraction, $1 - f_{\mathrm{UV}}$ is attributed to a spatially uniform UV background arising from faint galaxies with a typical separation much less than the mean free path of ionising photons. The flux power spectrum template is built from a set of 3 models variations with $f_{\mathrm{UV}} = 0, 0.5, 1$ where $f_{\mathrm{UV}} = 0$ corresponds to a spatially uniform UV background. Note, however, that a comprehensive treatment of spatial UV (and temperature, which we neglect here) fluctuations would require computationally prohibitive radiative transfer calculations in large volumes. As discussed in [25] spatial variations in the IGM temperature [37], mean free path [38] and fluctuations from bright Lyman break galaxies at high redshift [39] (particularly at $z > 5$) may also have an uncertain impact on the flux power.

Last but not least, we also vary the mean flux (or equivalently amplitude of the UV background) by rescaling $\tau_{\mathrm{eff}} = -\ln \bar{F}$. We use three different values $(0.8, 1, 1.2) \times \tau_{\mathrm{obs,eff}}$, with the reference values of $\tau_{\mathrm{obs,eff}}$ chosen to be those of the SDSS-III/BOSS measurements [19]. The mean flux evolution derived from the SDSS-III/BOSS analysis has values that are 5-8% lower compared to those measured by [34], but note that the range of values considered in our analysis brackets the observed values by [34] as well.

Finally, a few lower resolution simulations have also been run to check convergence and a single 1 keV WDM model has been considered to check the validity of the method described below. Each simulation used about 20,000 CPU hours. The total grid consists of 23 simulations at the reference resolution and 10 simulations at lower resolution.

IV. METHOD

Using the models of the transmitted flux obtained from the simulations we establish a grid of points for each redshift, in the parameter space of $(\bar{F}(z), T_0(z), \gamma(z), \sigma_8, z_{\rm rei}, n_{\rm eff}, f_{\rm UV}, m_{\rm WDM})$. We then perform a linear interpolation between the grid points in this multidimensional parameter space. The interpolation is done in the $P_{\rm F}(k, z)$ space directly, rather than for ratios of flux power spectra as in [7]. We perform several tests of the interpolation scheme (by predicting the value of the flux power at a given grid point where exact values are known, without using that grid point in the interpolation) and conclude that while a small systematic error due to interpolation exists ($< 5\%$ of the flux power spectrum), it does not bias the results. Additional tests were done when including this correction in the error budget of the likelihood estimation and results were unchanged. This reflects the fact that the interpolation error is small compared to the statistical error and sub-dominant in the systematic error budget of the current data. A Gaussian likelihood estimation was then used to evaluate a Monte Carlo Markov Chain (MCMC) algorithm to obtain the set of parameters that minimizes the likelihood for a given data set.

To estimate the convergence, four independent chains were run from randomly chosen initial set of parameters with different seed values for pseudo-random number generators. Using the Gelman-Rubin test on all of the chains we concluded that the chains have converged sufficiently (for each of the parameters the Gelman-Rubin measure of convergence was required to be less than 1.1). The resulting chains were combined after pruning the burn-in samples, from which the estimates of the posterior distributions (and its moments) were obtained.

V. RESULTS

We performed a detailed MCMC analysis for three different data sets: XQ-100 (the new data set), HIRES/MIKE (as in [7]) and the combined data sets. For the reference analysis case we model the mean flux parameters independently for each redshift bin, the number of which varies for each data set (XQ-100 has 7, MIKE/HIRES has 4 and the combined analysis has 10 redshift bins). We complement these parameters with an additional 9 parameters: 5 parameters describing either cosmology or astrophysics (σ_8, $n_{\rm eff}$, $z_{\rm rei}$, $m_{\rm WDM}$, $f_{\rm UV}$) and 4 parameters describing the thermal state of the IGM, using a power-law $T - \rho$ relation, $T = T_0 \Delta^{\gamma-1}$. Unless otherwise noted we model the redshift evolution of the parameters T_0 and γ as power-laws, such that $T_0(z) = T_0^A \left[(1+z)/(1+z_{\rm p})\right]^{T_0^S}$ and $\gamma(z) = \gamma^A \left[(1+z)/(1+z_{\rm p})\right]^{\gamma^S}$. The pivot redshift is different for each data set and roughly corresponds to the redshift at which most of the Lyman-α forest pixels are coming

from ($z_{\rm p} = 3.6, 4.5, 4.2$ for XQ-100, HIRES/MIKE and the combined analysis, respectively). As we will see later the choice of thermal priors significantly affects the results.

A default set of priors was used in the reference runs for the mean flux ($\bar{F}$) in each redshift bin, according to the $\tau_{\rm eff}$ fit to the data presented in [7], with 0.04 standard deviation (1σ). These priors account for the fact that different continuum treatments and different measurements give a slightly different normalization for the mean flux. The chosen fit roughly represents the median values of the observations (see [29]), with the 1σ standard deviations capturing the uncertainty in the normalization given by different measurements.

For all three data sets, the preferred ranges of other parameters are in agreement with independent observations. In particular the values of cosmological parameters σ_8 and $n_{\rm eff}$ are consistent with the latest Planck results within 1σ for XQ-100 and HIRES/MIKE and within 2σ for the combined analyses of XQ-100 and HIRES/MIKE. We have furthermore verified that the moderate 2σ discrepancy in σ_8 (and to lesser extent in $n_{\rm eff}$) can be alleviated by using additional priors on the above parameters. The applied priors were Gaussian on σ_8 and $n_{\rm eff}$ of ± 0.01 (1σ) around Planck values. Our measurements of the cosmological parameters are consistent with those measured by SDSS/BOSS collaboration [19], and moreover also show a similar tendency towards slightly higher values of σ_8 and slightly lower values of $n_{\rm eff}$.

It is also important to emphasise that the redshift coverage of XQ-100 and the higher resolution HIRES/MIKE data sets is mostly complementary (covering lower and higher redshifts respectively) and thus different constraints and degeneracies are expected in each. Even though XQ-100 covers a similar redshift range as the SDSS-II and SDSS-III Lyman-α power spectrum measurements, it extends to significantly smaller scales and should carry more information from the thermal cut-off in the flux power-spectrum. Note that the thermal cut-off is fixed in comoving co-ordinates in real space, while the cut-off in the observed transmitted flux power spectrum scales as $H(z)/(1+z)$ in velocity space. At a fixed velocity scale this means smaller comoving length scales (and thus free streaming lengths) are probed with increasing redshift. As a result, higher redshift data are more sensitive to the equivalent larger WDM relic mass than lower redshift data, where the effect of the thermal motions dominates already at larger comoving length scales. Measurements of WDM from lower redshift data, like those obtained from SDSS/BOSS flux power spectra, are thus mostly sensitive to the change of the power spectrum amplitude on the large scales, instead of probing the shape and redshift evolution of the free-streaming cut-off. In our analysis, this is supported by the fact that large degeneracies are found in our MCMC analysis for XQ-100 between the WDM mass and the values of the mean flux at each redshift (see Fig. A.1 in the appendix). Furthermore, since XQ-100 consists of fewer QSO spectra,
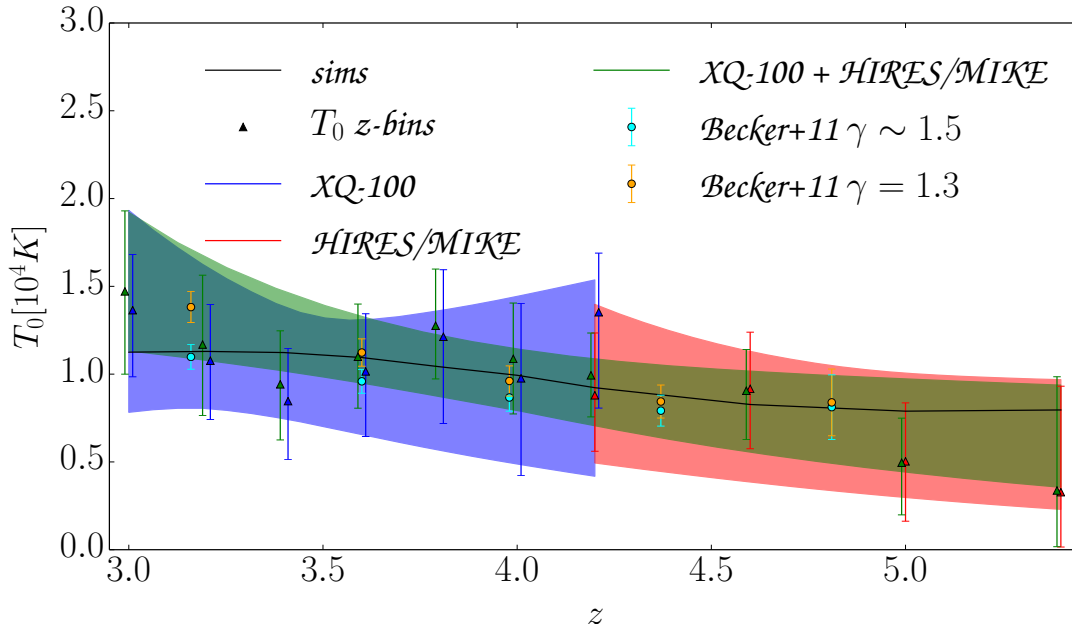
FIG. 1: Temperature measurements (2σ) as a function of redshift: reference simulation (black curve), XQ-100 (shaded blue area), HIRES/MIKE (shaded red area), joint constraints (shaded green area); points (same color coding) represent measurements obtained using T_0 in redshift bins, limiting temperature variations to $\Delta T = 5000\,\mathrm{K}$ between adjacent bins, rather than assuming a power-law evolution. Cyan and orange points with error bars are the IGM temperature measurements from [34] for two values of the slope of the temperature-density relation, $\gamma = 1.3$ and 1.5.

the error bars are larger than that of the SDSS measurements, which is why we do not expect the results from XQ-100 alone to constrain the WDM mass as tightly as various SDSS measurements.

Before discussing our new free-streaming constraints, in Fig. 1 we show the temperature estimates from our MCMC analysis of the flux power spectrum for the different data sets as 2σ shaded regions, assuming the temperature of the IGM varies smoothly with redshift as a power-law. In addition, we show individual points with 2σ errorbars that are obtained by allowing the temperature to float freely from bin to bin, but with a maximum temperature jump between bins of $\Delta T = 5000\,\mathrm{K}$ (discussed further below). Both results are in good agreement with the measurements of [34] obtained from the curvature of the transmitted flux, shown as orange and cyan points for two different assumptions for the power-law slope γ of the temperature-density relation (but note that these measurements were calibrated with hydrodynamical simulations where the dark matter was assumed to be cold). While our measurements are consistent with no evolution in temperature in the redshift range $3 < z < 5.4$, the preferred slope is negative (temperature increasing with decreasing redshift), which is in agreement with HeII reionisation occuring somewhere around redshifts $3 - 4$ as inferred from high-resolution Lyman-α forest data [40–43].

Earlier measurements of the IGM temperature at $z = 3$–4.3 by [40] using a Voigt profile fitting approach are also in reasonable agreement with our XQ-100 constraint (blue shading), although the error bars are large in that study. More recently, Ref. [41] measured $T_0 \simeq 26,000 \pm 5000\,\mathrm{K}$ (2σ) at $z = 3.4$ using wavelets, a result which is in greater tension with our measurement. This suggests there are still some systematic differences between these analyses likely associated with the calibration of hydrodynamical simulations and observational data. Note also that higher gas temperatures will in general raise the lower limit on the WDM particle mass and tighten the constraint further, so in this sense our constraint can be considered conservative.

Table 1 presents our marginalized parameter constraints, and Fig. 2 shows our constraints on the free-streaming of dark matter expressed as the mass of a putative thermal relic WDM particle. As expected the results from the XQ-100 data set alone (solid blue curve) only weakly constrain the mass ($m_{\mathrm{WDM}} > 1.4$ keV at 2σ). While the peak of the likelihood is not at 0, the peak is not statistically significant (not even at 1σ). Moreover, the exact position of the peak is strongly dependent on the choice of priors. However, the 2σ upper limit for $1/m_{\mathrm{WDM}}$ is nearly independent of prior choice, and constitutes a very robust measurement. We also show the case where a correction factor of 1.3 has been applied to

the covariance matrix and with weak priors on cosmological parameters (σ_8 and n_{eff} have Gaussian priors of $\pm$ 0.1 (1σ) around Planck values and the assumed temperature T_0^A is $10,000 \pm 5000$ K (1σ)). When we move to the model with with freely floating $T(z)$ bins rather than a power-law evolution of the temperature the free-streaming length inferred from the XQ-100 sample does not change.

Constraints on the WDM mass using the HIRES/MIKE sample were first presented in [7]. Compared to the analysis presented in [7] the main improvements in this work are as follows: the reference simulations have higher resolution and better coverage of parameter space, the model of spatial UV fluctuations has been extended, the interpolation scheme is based on the prediction of flux power rather than flux power ratios, and the (now one) cosmological parameter describing the slope of the power spectrum is closer to what is constrained by the data (n_{eff} rather than Ω_{m} and n_{s}).

We furthermore explored more physical priors for the evolution of the temperature that do not allow sudden, large jumps in the temperature. For reference, we have repeated the analysis in [7]) with the reference priors (and thermal history parameterized as a power law) used here and found that the the lower limit on m_{WDM} increases, from > 3.3 keV to > 3.9 keV (with the same Planck priors on σ_8 and n_{s} as used by [7]) and > 4.1 keV (with the reference priors used in this work).

The Planck prior used puts a Gaussian prior of ± 0.01 (1σ) around Planck values for σ_8 and n_{eff}. The result appears thus quite robust to changes in the choice of prior in cosmological parameters and details of the analysis but is sensitive to the assumed thermal priors. If we drop the assumption of a power-law evolution for the temperature of the IGM we get a lower bound of $m_{\text{WDM}} > 3.8$ keV.

This is a stronger limit than obtained by [7] in their analysis of the HIRES/MIKE data, as well as in a more recent reanalysis of the same data by [44] that further relaxed assumptions regarding the IGM temperature evolution. This is because we have limited the change in temperature jumps between redshift bins of $\Delta z = 0.2$–0.4 to a physically plausible value of $\Delta T = 5000$ K. Any change in the (volume averaged) IGM temperature over $3 < z < 5.4$ will be due to either photo-heating of the IGM during (QSO driven) HeII reionisation or adiabatic cooling due to the expansion of the Universe. Models that follow the expected HeII ionising emissivity and spectral shape of quasars are consistent with temperature boosts of at most $\Delta T = 5000$–10000 K which are gradual and occur over $\Delta z \gtrsim 1$ [42, 43, 45]. The same holds for a plausible drop in the temperature due to adiabatic cooling, which (ignoring heating) will at most scale as $T_0 \propto (1 + z)^2$. Larger values of ΔT are not readily achievable within physically motivated reionization models. For this reason, [7] strongly disfavored the binned analysis they performed for completeness that weakened their constraint by around 1 keV.

Our analysis of the combined data sets also gives significantly strengthened constraints on the WDM mass, driven mostly again by the high redshift HIRES/MIKE data set. However, unlike combining the above data set with SDSS (as in [7] where the inclusion of SDSS-II data did not impact on the free-streaming constraints), our combined analysis of the high-redshift, high-resolution data with the XQ-100 sample gives a significantly stronger lower limit on m_{WDM}. This is again mostly due to the more physical temperature evolution that we assumed when combining the two data sets, that does not allow for sudden jumps in the temperature evolution. We expect that were such a prior on the temperature evolution used also in the case when combining SDSS-II with HIRES/MIKE, that a stronger bound on the WDM mass would also be obtained.

Much like in our analysis of the HIRES/MIKE only data set, the results for the combined data sets is – apart from the thermal priors – largely independent of the choices of prior and thus robust. For the combined data sets the 2σ C.L. lower limit is 5.3 keV. This limit again weakens if we use the freely-floating temperature bins rather than a power law to 3.5 keV. The same priors were used in this analysis as for the HIRES/MIKE only analysis, with an upper limit on the difference in temperature between adjacent redshift bins again of $\Delta T = 5000$ K.

Parameter	XQ-100	HIRES/MIKE	Combined
m_{WDM} [keV]	> 1.4	> 4.1	> 5.3
σ_8	$[0.75, 0.92]$	$[0.75, 1.32]$	$[0.83, 0.95]$
n_{eff}	$[-2.42, -2.25]$	$[-2.53, -2.11]$	$[-2.43, -2.32]$
$T^A(z_{\text{p}})$ [10^4 K]	$[0.73, 1.27]$	$[0.46, 1.12]$	$[0.74, 1.06]$
$T^S(z_{\text{p}})$	$[-4.39, 1.89]$	$[-4.78, -1.80]$	$[-3.22, -0.82]$
$\gamma^A(z_{\text{p}})$	$[1.12, 1.45]$	$[1.08, 1.52]$	$[1.23, 1.69]$
$\gamma^S(z_{\text{p}})$	$[-1.89, 0.17]$	$[-1.18, 1.77]$	$[-0.07, 1.81]$
z_{rei}	$[6.5, 15.66]$	$[6.26, 14.88]$	$[6.25, 13.43]$
f_{UV}	$[0.06, 0.96]$	$[0.05, 0.96]$	$[0.05, 0.94]$
$\chi^2/d.o.f.$	$134/124$	$33/40$	$185/173$

TABLE I: Marginalized constraints at 95 %. Pivot redshifts for different data sets are: $z_p = 3.6, 4.5, 4.2$ for XQ-100, HIRES/MIKE and combined.

VI. CONCLUSIONS

We have presented new constraints on the free-streaming of WDM based on an MCMC analysis of the XQ-100 and HIRES/MIKE Lyman-α forest data sets. The new constraints in terms of the mass of a thermal relic WDM particle, $m_{\text{WDM}} > 5.3$ keV at 2σ, are the strongest to date, and thus imply significantly colder dark matter than the $2 - 2.5$ keV values that are typically required to mitigate tensions in the predictions of cold dark matter models with other astrophysical observations on small scales.
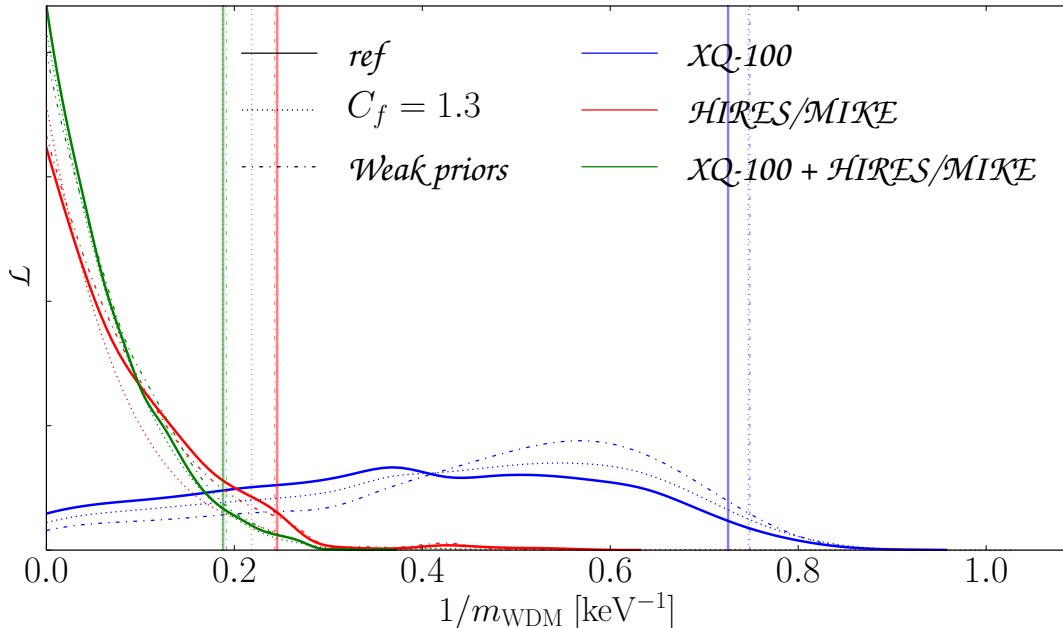
FIG. 2: One dimensional posterior likelihood distributions for the WDM mass for XQ-100, HIRES/MIKE and the combined data (blue, red and green solid curves). We also show how the results change by using a larger value for the correction factor of the XQ-100 covariance matrix (dotted curves) and using weak priors (see text) on the thermal history and cosmological parameters (dot-dashed curves). Vertical lines show the corresponding 2σ confidence limits.

Previous analysis of the same high-resolution Lyman-α forest data had given constraints of $m_{\rm WDM} > 3.3$ keV ([7] using HIRES/MIKE) and > 3.95 keV ([8]; using SDSS-III/BOSS). Adding the new data from the XQ-100 survey which has similar redshift coverage as SDSS, but extends to significantly smaller scales, has strengthened the constraints to a significantly smaller free-streaming length and corresponding larger values of the mass of a thermal relic WDM particle. Another important aspect of our new analysis was the assumption of more physical priors on the gas temperature evolution with redshift. While the results of our analysis for the new XQ-100 data alone give relatively weak constraints, the combined analysis is very robust to different choices of priors and also gives a largely consistent picture with independent, more direct measurements of the the thermal history of the IGM over a wide redshift range $z = 3 - 5.4$ [34]. This is due to the complementarity of the XQ-100 and MIKE/HIRES data sets in redshift and the corresponding longer "lever arm" of the combined sample in redshift. On large scales the main degeneracies are between the mean flux, gas temperature and the amplitude of matter fluctuations. At the lower redshifts probed by the moderate resolution XQ-100 data, the WDM constraints are coming predominantly from these scales and are therefore coupled to the same degeneracies. On small scales, however, the cut-off in the flux power spectrum is dominated by thermal, Jeans or WDM smoothing, which introduces a dif-

ferent set of degeneracies. At higher redshifts the WDM smoothing scale increases relative to the thermal/Jeans smoothing scale in velocity space, thus most constraining power comes from small scales at high redshift.

We conclude with three important remarks. First, the tightest limit presented here weakens if we drop the assumption of a power-law evolution for the temperature and use instead a thermal history with freely floating $T(z)$ bins (but with limited temperature jumps between adjacent bins) in our analysis. In this case the limit weakens to 3.5 keV, a number which is very similar to the one obtained from similar analyses of HIRES/MIKE data assuming a power-law evolution of the thermal parameters characterising the IGM [7]. Models with free-streaming lengths larger than this require, however, an unphysical heating and/or cooling of the IGM over a very short short timescale, in strong disagreement with theoretical expectations for the IGM thermal history and measurements of the IGM temperature based on high-resolution Lyman-α forest data.

Secondly, [25] have recently suggested that temperature fluctuations could compensate for the WDM cutoff by providing an increase of power at small scales (but see also [46]). This is potentially an important systematic effect that should be better quantified by performing template fitting based on more accurate modelling of spatial fluctuations of the meta-galactic UV background, as well as the residual temperature fluctuations from hydrogen

reionization with radiation hydrodynamical simulations that incorporate radiative transfer effects rather than analytical modeling.

Thirdly, it should (at least in principle) be possible to further (moderately) strengthen the limits on the free-streaming of warm dark matter by reducing the statistical errors of the high-redshift, small scale flux power spectrum obtainable with high-resolution spectrographs and further constraining the thermal and reionization history of the IGM.

Appendix A: Parameter degeneracies

Degeneracies between the parameters play an important role in how well a specific parameter (e.g. free streaming length/WDM mass) can be estimated using different data sets. In the bottom row of Fig. A.1, it is clear that for low redshift data (XQ-100; blue coloured contours), there are strong degeneracies between the mass of a thermal relic WDM particle and the temperature (at a given redshift). This is not surprising, since both the temperature and WDM effects change the power spectrum on large as well as small scales. At lower redshifts the effects are small in both cases and thus harder to distinguish within the observational errorbars. The degeneracy with temperature is an anti-correlation that is expected; the data prefers either higher temperatures and lower masses of WDM, or lower temperatures with higher WDM masses.

However, whereas the temperature degeneracy with the free streaming length comes as no surprise, the mean flux degeneracy might not be naively expected (bottom left panel of Fig. A.1). Since this degeneracy has a similar anti-correlation with the mass of the WDM as seen for the temperature (also shown as positive correlation between mean flux and temperature - top left 2D panel in Fig. A.1), it means the sensitivity of the XQ-100 data to the WDM mass comes mostly from the overall amplitude of the flux power spectrum, rather than its shape in the cutoff regime at smaller scales. A possible solution (apart from measuring different statistics, and increasing the precision of the current measurements) would be to increase the maximum scale up to which the flux power spectrum is measured. If the thermal/Jeans smoothing and smoothing due to a high WDM mass are different enough a feature (kink) should be observable on some (arbitrarily) small scales where the flux power spectrum cutoff transitions from being dominated by the thermal/Jeans smoothing to being dominated by the mass of the WDM. This would, however, only work if the WDM mass is large enough.

The above degeneracies almost disappear when using the higher redshift data in the analysis (HIRES/MIKE; red coloured contours). Fig. A.1 shows no appreciable degeneracy between mass of the WDM and any other parameters. This is because at higher redshifts, for the WDM masses we consider here the cutoff scale by the free-streaming of the WDM becomes more and more important and this scale will show no redshift evolution and will be thus easier to pick up in the data. This is the reason why the higher redshift data becomes such a powerful tool for constraining the free-streaming. To increase the constraining power, more observations to decrease the statistical errors would be more beneficial than pushing to smaller scales (although the latter would be helpful as well). This is because the MCMC analysis shows that the constraints on the free-streaming length are largely independent of the different assumed values of priors, meaning that the resulting lower bound on the mass of the WDM is driven by the statistical error.

Lastly we draw attention to a slight discrepancy in the measurement of the slope of the $T - \rho$ relation (third row of Fig. A.1). The value of $\gamma(z = 4.2)$ measured from the low and high redshift data sets are in modest $(1 - 2\sigma)$ tension. While this could be a statistical fluke, we would like to point out that this might actually be an expected result, if HeII reionization happens somewhere between redshift $3 - 4$. The high redshift data (HIRES/MIKE) measures the thermal history above a redshift of $z = 4.2$, where HeII reionization (that happens at lower redshifts) would have little effect. The value of γ at these redshifts is thus expected to slowly increase and approach the asymptotic value of around 1.6 [40, 42, 43]). The evolution is well described by a power-law in redshift. However, with HeII reionization somewhere between $z = 3-4$, a feature is to be expected in the evolution of γ, where its value falls to $\gamma = 1.2$–1.3 and then start to rise again towards higher asymptotic values over a redshift interval of $\Delta z \sim 2$ [42]. If we fit such a feature with a simple power-law in redshift, a lower amplitude for the power-law would be obtained compared to the case where there is no feature in the evolution, and no HeII reionization. This is what the data is preferring - higher values of γ measured from high redshift data set, and lower overall amplitude of γ at lower redshifts. We note, however, that a more detailed model of $\gamma(z)$ evolution may be necessary at lower redshift to capture possible HeII reionization effects. Dropping the assumption of a simple power-law describing the evolution of $T_0(z)$ and $\gamma(z)$, and allowing for the power-law evolution to have different slope below and above $z_p = 4.2$, relaxes this tension considerably, as is shown in the third row of Fig. A.1 (magenta colour – double powerlaw). The WDM constraints in this case are slightly weaker compared to the reference case of the analysis of the combined data sets, and exclude WDM masses above $m_{\rm WDM} > 4.5$ keV. The tension disappears for the case of using T_0 in independent redshift bins, even though $\gamma(z)$ is still described as a single power-law in such a case. The WDM limits derived from this case are described in the main text.
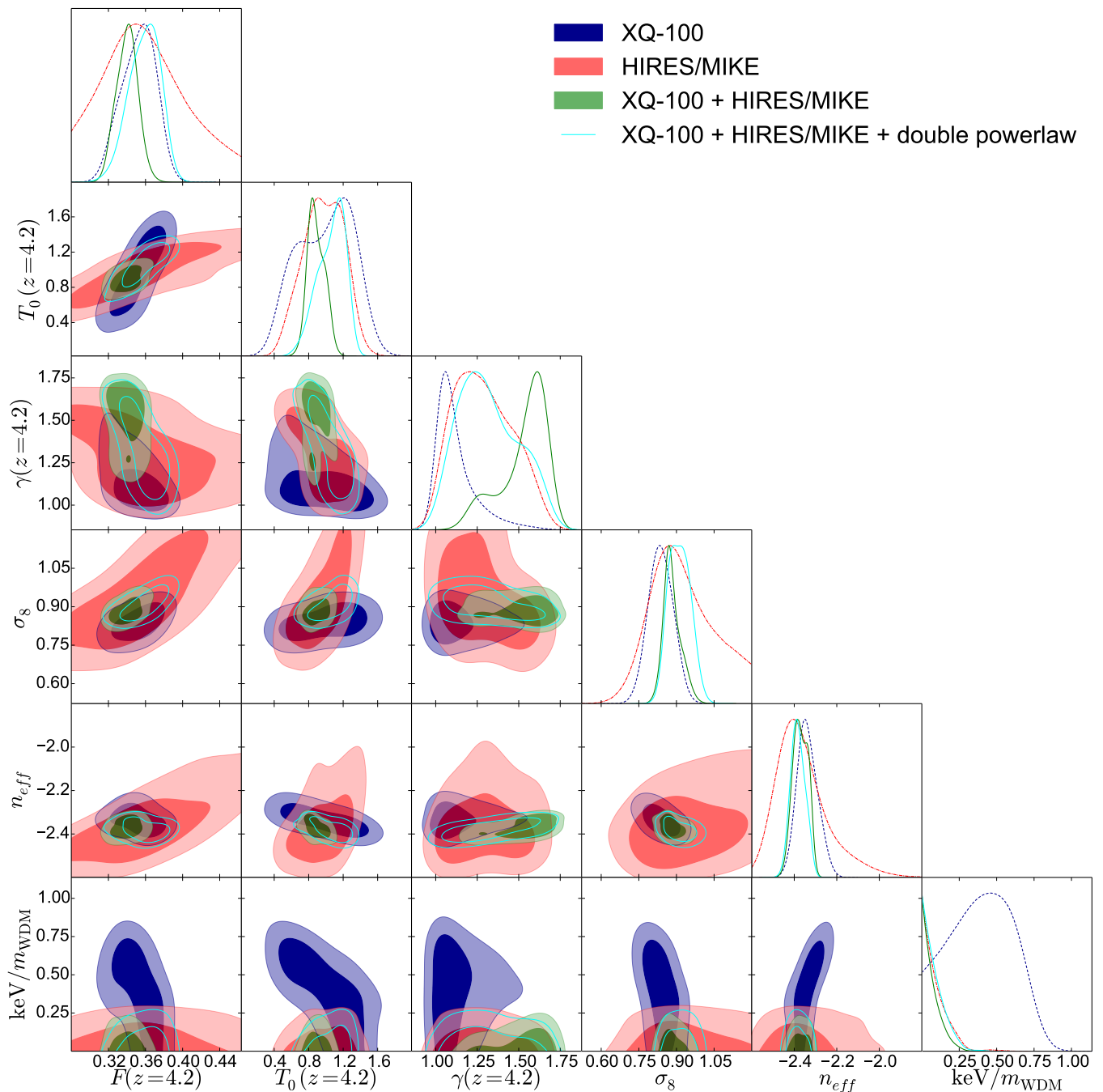
FIG. A.1: Two dimensional posterior (marginalized) likelihood distributions for the main parameters for the XQ-100, HIRES/MIKE and combined data sets (blue, red and green curves), respectively. We also show contours when using a double power-law evolution of the thermal parameters (cyan curves), as described in more details in the text. Instead of 4 parameters describing the thermal history only values evaluated at a specific redshift were chosen. The redshift chosen is where different data sets overlap.

Appendix B: Degeneracy between WDM mass and redshift of reionization

Due to the fact that smoothing from both WDM thermal relic as well as pressure smoothing act on the 3D matter power spectrum a certain amount of degeneracy between the parameters is expected. However, in this section we show that this degeneracy is largely broken by the long redshift range considered in the data analysis.
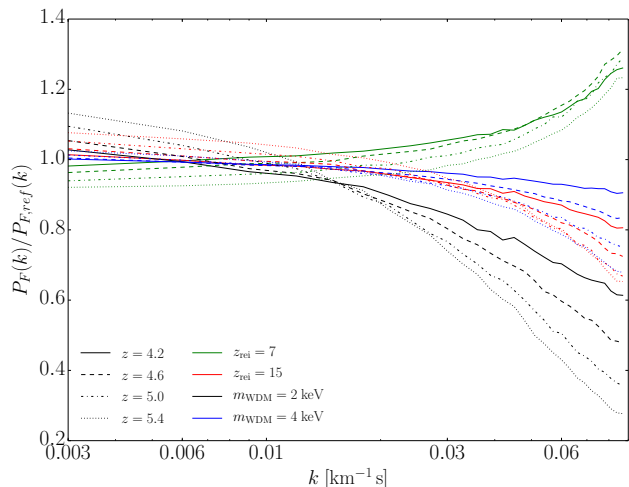
FIG. B.2: The flux power spectrum for different models varying mass of the WDM (m_{WDM}) and redshift of reionization (z_{rei}). The colours show two values of m_{WDM} - 2 keV in blue and 4 keV in black - and two values of z_{rei} - 7 in green and 15 in red. The reference model against which the flux power is compared, was ΛCDM model with $z_{\text{rei}} = 9$. Different line styles show the redshift evolution of the flux power: full line ($z = 4.0$), dashed line ($z = 4.6$), dot-dashed line ($z = 5.0$) and dotted line ($z = 5.4$). Only the effect on the largest redshift bins is shown since that is where the effect of WDM on the smoothing scale becomes largest. The plot illustrates how the redshift evolution changes the shape of the flux power differently for the two parameters.
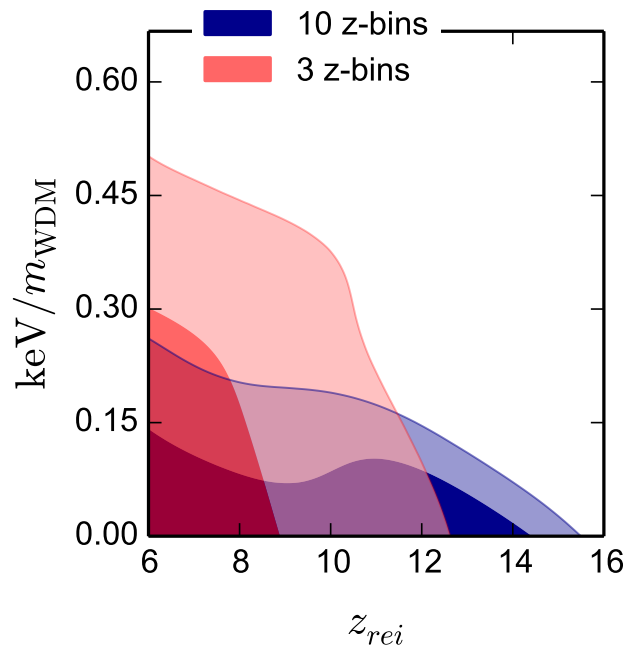

FIG. B.3: The 2D posterior likelihood contours in the parameter plane of mass of WDM particle and redshift of reionization. Different colours represent different subsets of the combined data set used. In particular, the blue colour shows the full analysis of the combined data (XQ-100 + HIRES/MIKE) which used 10 redshift bins. In red we show the results when only 3 redshift bins were used in the analysis, centered around $z = 4.2$ ($z = 4.0, 4.2, 4.6$).

Fig. B.2 shows the flux power ratio when we vary WDM and z_{rei} models compared to the reference ΛCDM case. The plot nice nicely illustrates how the different redshift evolution of the effect of reionization redshift and free-streaming of the dark matter on the flux power spectrum makes it possible to separate the two effects. To fully capture the effect these two degenerate parameters have, we used used a grid of simulations that samples the parameter plane of $1/m_{\text{WDM}}$ and z_{rei}.

To illustrate the effect of redshift evolution further, we show a 2D plot of the posterior likelihood distribution in the parameter plane of m_{WDM} and z_{rei} (Fig. B.3). The degeneracy between the two parameters is increased when only three redshift bins are considered in the analysis. These redshift bins also do not span the whole length of the redshift range the combined data set tracks, but are centered around the pivot redshift of $z = 4.2$ ($z = 4.0, 4.2, 4.6$).

Furthermore, in Fig. B.4 we show the redshift evolution of the different smoothing scales that affect the cut-off in the flux power spectrum. We have used the thermal history evolution of our reference model in the case of thermal, Jeans and filtering scale. The filtering scale shown on this plot was computed using the relation in [47] - i.e. $\lambda_F = 2\pi/k_F$. We also show the Jeans smooth-

ing scale since it has been argued in [47] that the filtering scale λ_F will always be smaller than the Jeans scale λ_J. Thus the Jeans scale plays a role of a (conservative) upper limit on the amount of pressure smoothing. The plot shows that thermal and filtering (or Jeans) scales have a very different redshift evolution compared to the free-streaming scale of the warm dark matter, which is the only scale slowly increasing with redshift in velocity space. Fig. B.4 is meant to be of illustrative purpose only, to show that different scales evolve differently with redshift. We would also like to caution the reader that, while the pressure smoothing scale (Jeans or filtering) and WDM free-streaming scale, are acting on the 3D matter density field, the thermal scale is a 1D smoothing scale that operates on the optical depth field.

While Fig. B.4 shows that the redshift evolution differs between different smoothing scales, the MCMC bounds derived in this paper make use of the full shape of the flux power spectrum. Furthermore, the flux power spectrum traces the integral over the 3D matter power, and is thus sensitive to small scales at any given parallel wavenumber. Indeed, this is why lower resolution surveys are also able to put bounds on the WDM free-streaming scale [8]. The effect of redshift evolution on the shape of the flux power spectrum is shown in Fig. B.5. Even on large
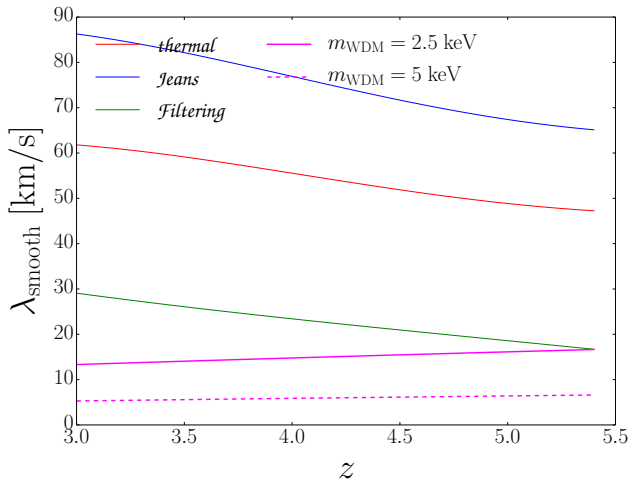
FIG. B.4: The redshift evolution of the different smoothing scales in units of $\mathrm{km\,s^{-1}}$: thermal (red), Jeans (blue), filtering (green) and free-streaming from WDM thermal relic (magenta). The two line-styles show different values of the WDM mass for 2.5 keV (full line) and 5 keV (dashed line) respectively.
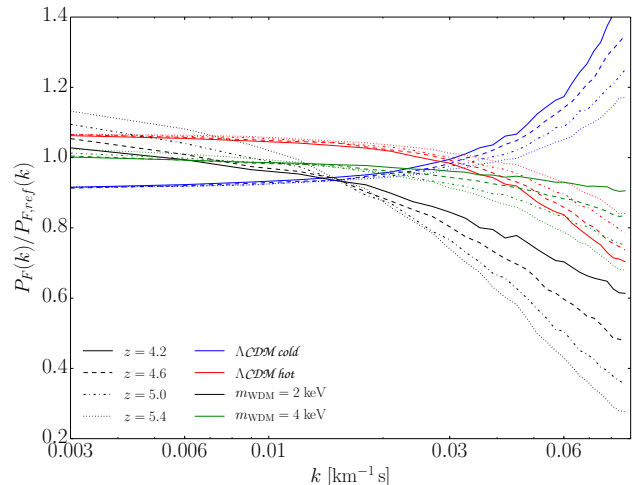

FIG. B.5: The flux power spectrum for different models varying mass of the WDM (m_{WDM}) and the amplitude of the IGM temperature at the mean density (T_0^A). The colours show two values of m_{WDM} - 2 keV in black and 4 keV in green - and two ΛCDM models with different temperatures - hot IGM in red (roughly 3000K hotter) and cold in blue (roughly 3000K colder). The reference model against which the flux power is compared, was ΛCDM model with $T_0(z = 3.6) = 11000$K. Different line styles show the redshift evolution of the flux power: full line ($z = 4.0$), dashed line ($z = 4.6$), dot-dashed line ($z = 5.0$) and dotted line ($z = 5.4$). As with Fig. B.2, only the effect on the largest redshift bins is shown since that is where the effect of WDM on the smoothing scale becomes largest.

scales ($k < 0.01\,\mathrm{s\,km^{-1}}$), models with varying amount of thermal or WDM free-streaming smoothing have quite distinct shapes. Combining the shape with the redshift evolution helps break the degeneracies among the IGM parameters and the mass of the WDM.

Appendix C: The effect of different priors on the limits of m_{WDM}

In this section we show an extended table of how the limits on the mass of the WDM change when imposing different priors. The priors for reference case and weak priors are the same as the ones plotted in Fig. 2.

The reference priors consist of weak priors on the values of mean flux in each redshift bin. These priors were chosen to be Gaussian with mean value as predicted by the empirical fit by [19] with $\pm$ 0.04 (1σ). Further, the reference priors include bounds on some of the parameters that are physically motivated: $m_{\mathrm{WDM}} \geq 0$, $6 \leq z_{\mathrm{rei}} \leq 16$, 0 K $\leq T_0^A \leq 20000$ K, $-5 \leq T_0^S \leq 5$ and $1 \leq \gamma(z_i) < 1.7$ for each redshift z_i. We have also checked that the exact values for upper and lower bounds on z_{rei} and the temperature amplitude (T_0^A) and slope (T_0^S) do not have an impact on the final constraints of the WDM. The bounds for γ at each redshift are physically motivated for the time of HeII reionization [1, 48].

The weak priors, as already described in the main body of the text, add the following priors to the reference values: σ_8 and n_{eff} have Gaussian priors of $\pm$ 0.1 (1σ) around Planck values and the assumed temperature T_0^A is 10000 ± 5000 K (1σ).

Priors used	XQ-100	HIRES/MIKE	Combined
Reference	> 1.38	> 4.08	> 5.32
Weak priors	> 1.33	> 4.11	> 5.21
Planck priors	> 1.34	> 3.95	> 5.25
Thermal priors	> 1.49	> 2.11	> 3.48

TABLE II: Marginalized constraints at 95 % for m_{WDM} in the units of keV. Different priors used are the reference case, weak priors, Planck priors on the cosmological parameters and physical priors on thermal evolution where T_0 varies freely with redshift bins. Compared to the result shown in Table I more decimal points are shown in the result.

Furthermore, priors on cosmological parameters were added to the reference once (Planck priors), such that: σ_8 and n_{eff} have Gaussian priors of $\pm$ 0.01 (1σ) around Planck values.

And lastly, we also considered a temperature evolution where the temperature T_0 was allowed to vary freely in each of the redshift bins. In this case we have used references values for priors to which we have added additional constraint on the change of the temperature between redshift bins, such that the change in temperature jumps between redshift bins of $\Delta z = 0.2$–0.4 was limited to a

physically plausible value of $\Delta T = 5000\,\mathrm{K}$.

Appendix D: Bestfit and confidence levels tables

In this section we show the full tables of the best-fit parameters (and their 1 and 2σ confidence intervals) for the MCMC analysis of the three different data sets: XQ-100 (Table S1), HIRES/MIKE (Table S2) and combined XQ-100 + HIRES/MIKE (Table S3).

Parameter	(1σ)	(2σ)	Best fit
$\bar{F}(z=3.0)$	$[0.67, 0.68]$	$[0.65, 0.70]$	0.68
$\bar{F}(z=3.2)$	$[0.61, 0.62]$	$[0.59, 0.64]$	0.61
$\bar{F}(z=3.4)$	$[0.54, 0.56]$	$[0.53, 0.57]$	0.55
$\bar{F}(z=3.6)$	$[0.50, 0.51]$	$[0.49, 0.53]$	0.51
$\bar{F}(z=3.8)$	$[0.44, 0.45]$	$[0.41, 0.46]$	0.44
$\bar{F}(z=4.0)$	$[0.38, 0.39]$	$[0.36, 0.41]$	0.39
$\bar{F}(z=4.2)$	$[0.34, 0.36]$	$[0.32, 0.38]$	0.35
$T_0^A(z=z_p)$ [10^4 K]	$[0.97, 1.12]$	$[0.73, 1.27]$	1.03
$T_0^S(z=z_p)$	$[-1.54, 0.73]$	$[-4.39, 1.89]$	-0.69
$\gamma^A(z=z_p)$	$[1.25, 1.31]$	$[1.12, 1.45]$	1.28
$\gamma^S(z=z_p)$	$[-1.55, -0.97]$	$[-1.89, 0.17]$	-1.14
σ_8	$[0.81, 0.86]$	$[0.75, 0.92]$	0.84
z_{rei}	$[9.92, 13.47]$	$[6.50, 15.66]$	11.50
n_{eff}	$[-2.36, -2.32]$	$[-2.42, -2.25]$	-2.34
$1/m_{\mathrm{WDM}}$ [keV^{-1}]	$[0, 0.63]$	$[0, 0.77]$	0.40
f_{UV}	$[0.36, 0.72]$	$[0.06, 0.96]$	0.53

TABLE III: XQ-100: Marginalized constraints at 68 and 95 %, obtained from the MCMC analysis as well as bestfit values. The pivot redshift is $z_{\mathrm{p}} = 3.6$.

Parameter	(1σ)	(2σ)	Best fit
$\bar{F}(z=4.2)$	$[0.33, 0.38]$	$[0.27, 0.46]$	0.36
$\bar{F}(z=4.6)$	$[0.25, 0.29]$	$[0.21, 0.37]$	0.27
$\bar{F}(z=5.0)$	$[0.14, 0.17]$	$[0.12, 0.21]$	0.16
$\bar{F}(z=5.4)$	$[0.04, 0.06]$	$[0.03, 0.08]$	0.05
$T_0^A(z=z_p)$ [10^4 K]	$[0.71, 0.91]$	$[0.46, 1.12]$	0.80
$T_0^S(z=z_p)$	$[-3.93, -3.11]$	$[-4.78, -1.80]$	-3.46
$\gamma^A(z=z_p)$	$[1.22, 1.38]$	$[1.08, 1.52]$	1.30
$\gamma^S(z=z_p)$	$[-0.28, 0.81]$	$[-1.18, 1.77]$	0.25
σ_8	$[0.86, 1.01]$	$[0.75, 1.32]$	0.96
z_{rei}	$[8.44, 11.52]$	$[6.26, 14.88]$	10.12
n_{eff}	$[-2.43, -2.33]$	$[-2.53, -2.11]$	-2.36
$1/m_{\mathrm{WDM}}$ [keV^{-1}]	$[0, 0.17]$	$[0, 0.28]$	0.09
f_{UV}	$[0.35, 0.70]$	$[0.05, 0.96]$	0.52

TABLE IV: HIRES/MIKE: Marginalized constraints at 68 and 95 %, obtained from the MCMC analysis as well as bestfit values. The pivot redshift is $z_{\mathrm{p}} = 4.5$.

Parameter	(1σ)	(2σ)	Best fit
$\bar{F}(z=3.0)$	$[0.69, 0.70]$	$[0.67, 0.71]$	0.69
$\bar{F}(z=3.2)$	$[0.62, 0.63]$	$[0.61, 0.64]$	0.63
$\bar{F}(z=3.4)$	$[0.56, 0.57]$	$[0.54, 0.58]$	0.56
$\bar{F}(z=3.6)$	$[0.51, 0.52]$	$[0.50, 0.53]$	0.52
$\bar{F}(z=3.8)$	$[0.45, 0.46]$	$[0.44, 0.47]$	0.45
$\bar{F}(z=4.0)$	$[0.38, 0.39]$	$[0.37, 0.40]$	0.38
$\bar{F}(z=4.2)$	$[0.33, 0.35]$	$[0.32, 0.36]$	0.34
$\bar{F}(z=4.6)$	$[0.25, 0.27]$	$[0.23, 0.29]$	0.26
$\bar{F}(z=5.0)$	$[0.13, 0.14]$	$[0.11, 0.17]$	0.13
$\bar{F}(z=5.4)$	$[0.03, 0.04]$	$[0.01, 0.06]$	0.04
$T_0^A(z=z_p)$ [10^4 K]	$[0.83, 0.94]$	$[0.74, 1.06]$	0.89
$T_0^S(z=z_p)$	$[-2.59, -1.99]$	$[-3.22, -0.82]$	-2.23
$\gamma^A(z=z_p)$	$[1.51, 1.63]$	$[1.23, 1.69]$	1.53
$\gamma^S(z=z_p)$	$[0.81, 1.42]$	$[-0.07, 1.81]$	1.04
σ_8	$[0.87, 0.89]$	$[0.83, 0.95]$	0.88
z_{rei}	$[8.21, 11.37]$	$[6.25, 13.43]$	9.80
n_{eff}	$[-2.39, -2.35]$	$[-2.43, -2.32]$	-2.37
$1/m_{\mathrm{WDM}}$ [keV^{-1}]	$[0, 0.13]$	$[0, 0.22]$	0.07
f_{UV}	$[0.32, 0.65]$	$[0.05, 0.94]$	0.48

TABLE V: Combined: Marginalized constraints at 68 and 95 %, obtained from the MCMC analysis as well as bestfit values. The pivot redshift is $z_{\mathrm{p}} = 4.2$.

---

[1] M. McQuinn. The Evolution of the Intergalactic Medium. *ArXiv e-prints*, November 2015.

[2] V. K. Narayanan, D. N. Spergel, R. Davé, and C.-P. Ma. Constraints on the Mass of Warm Dark Matter Particles and the Shape of the Linear Power Spectrum from the Lyα Forest. Astrophysical Journal Letters, 543:L103–L106, November 2000.

[3] M. Viel, J. Lesgourgues, M. G. Haehnelt, S. Matarrese, and A. Riotto. Constraining warm dark matter candidates including sterile neutrinos and light gravitinos with WMAP and the Lyman-α forest. *Phys. Rev. D* , 71(6):063534, March 2005.

[4] U. Seljak, A. Makarov, P. McDonald, and H. Trac. Can Sterile Neutrinos Be the Dark Matter? *Physical Review Letters*, 97(19):191303, November 2006.

[5] M. Viel, G. D. Becker, J. S. Bolton, M. G. Haehnelt, M. Rauch, and W. L. W. Sargent. How Cold Is Cold Dark Matter? Small-Scales Constraints from the Flux Power Spectrum of the High-Redshift Lyman-α Forest. *Physical Review Letters*, 100(4):041304, February 2008.

[6] S. Bird, H. V. Peiris, M. Viel, and L. Verde. Minimally parametric power spectrum reconstruction from the Lyman α forest. MNRAS, 413:1717–1728, May 2011.

[7] M. Viel, G. D. Becker, J. S. Bolton, and M. G. Haehnelt. Warm dark matter as a solution to the small scale crisis: New constraints from high redshift Lyman-α forest data. *Phys. Rev. D* , 88(4):043502, August 2013.

[8] J. Baur, N. Palanque-Delabrouille, C. Yèche, C. Magneville, and M. Viel. Lyman-alpha forests cool warm dark matter. J. Cosmology Astropart. Phys., 8:012, August 2016.

[9] R. A. C. Croft, D. H. Weinberg, M. Bolte, S. Burles, L. Hernquist, N. Katz, D. Kirkman, and D. Tytler. Toward a Precise Measurement of Matter Clustering: Lyα Forest Data at Redshifts 2-4. *Astrophys. J.* , 581:20–52, December 2002.

[10] M. Zaldarriaga, R. Scoccimarro, and L. Hui. Inferring the Linear Power Spectrum from the Lyα Forest. *Astrophys. J.* , 590:1–7, June 2003.

[11] P. McDonald. Toward a Measurement of the Cosmological Geometry at z ˜ 2: Predicting Lyα Forest Correlation in Three Dimensions and the Potential of Future Data Sets. *Astrophys. J.* , 585:34–51, March 2003.

[12] M. Viel, M. G. Haehnelt, and V. Springel. Inferring the dark matter power spectrum from the Lyman α forest in high-resolution QSO absorption spectra. MNRAS, 354:684–694, November 2004.

[13] P. McDonald, U. Seljak, R. Cen, D. Shih, D. H. Weinberg, S. Burles, D. P. Schneider, D. J. Schlegel, N. A. Bahcall, J. W. Briggs, J. Brinkmann, M. Fukugita, Ž. Ivezić, S. Kent, and D. E. Vanden Berk. The Linear Theory Power Spectrum from the Lyα Forest in the Sloan Digital Sky Survey. *Astrophys. J.* , 635:761–783, December 2005.

[14] U. Seljak, A. Slosar, and P. McDonald. Cosmological parameters from combining the Lyman-α forest with CMB, galaxy clustering and SN constraints. J. Cosmology Astropart. Phys., 10:14, October 2006.

[15] N. Palanque-Delabrouille, C. Yèche, J. Baur, C. Magneville, G. Rossi, J. Lesgourgues, A. Borde, E. Burtin, J.-M. LeGoff, J. Rich, M. Viel, and D. Weinberg. Neutrino masses and cosmology with Lyman-alpha forest power spectrum. J. Cosmology Astropart. Phys., 11:011, November 2015.

[16] N. G. Busca, T. Delubac, J. Rich, S. Bailey, A. Font-Ribera, D. Kirkby, J.-M. Le Goff, M. M. Pieri, A. Slosar, É. Aubourg, J. E. Bautista, D. Bizyaev, M. Blomqvist, A. S. Bolton, J. Bovy, H. Brewington, A. Borde, J. Brinkmann, B. Carithers, R. A. C. Croft, K. S. Dawson, G. Ebelke, D. J. Eisenstein, J.-C. Hamilton, S. Ho, D. W. Hogg, K. Honscheid, K.-G. Lee, B. Lundgren, E. Malanushenko, V. Malanushenko, D. Margala, C. Maraston, K. Mehta, J. Miralda-Escudé, A. D. Myers, R. C. Nichol, P. Noterdaeme, M. D. Olmstead, D. Oravetz, N. Palanque-Delabrouille, K. Pan, I. Pâris, W. J. Percival, P. Petitjean, N. A. Roe, E. Rollinde, N. P. Ross, G. Rossi, D. J. Schlegel, D. P. Schneider, A. Shelden, E. S. Sheldon, A. Simmons, S. Snedden, J. L. Tinker, M. Viel, B. A. Weaver, D. H. Weinberg, M. White, C. Yèche, and D. G. York. Baryon acoustic oscillations in the Lyα forest of BOSS quasars. A&A, 552:A96, April 2013.

[17] A. Slosar, V. Iršič, D. Kirkby, S. Bailey, N. G. Busca, T. Delubac, J. Rich, É. Aubourg, J. E. Bautista, V. Bhardwaj, M. Blomqvist, A. S. Bolton, J. Bovy, J. Brownstein, B. Carithers, R. A. C. Croft, K. S. Dawson, A. Font-Ribera, J.-M. Le Goff, S. Ho, K. Honscheid, K.-G. Lee, D. Margala, P. McDonald, B. Medolin, J. Miralda-Escudé, A. D. Myers, R. C. Nichol, P. Noterdaeme, N. Palanque-Delabrouille, I. Pâris, P. Petitjean, M. M. Pieri, Y. Piškur, N. A. Roe, N. P. Ross, G. Rossi, D. J. Schlegel, D. P. Schneider, N. Suzuki, E. S. Sheldon, U. Seljak, M. Viel, D. H. Weinberg, and C. Yèche. Measurement of baryon acoustic oscillations in the Lyman-α forest fluctuations in BOSS data release 9. J. Cosmology Astropart. Phys., 4:26, April 2013.

[18] K. S. Dawson, D. J. Schlegel, C. P. Ahn, S. F. Anderson, É. Aubourg, S. Bailey, R. H. Barkhouser, J. E. Bautista, A. Beifiori, A. A. Berlind, V. Bhardwaj, D. Bizyaev, C. H. Blake, M. R. Blanton, M. Blomqvist, A. S. Bolton, A. Borde, J. Bovy, W. N. Brandt, H. Brewington, J. Brinkmann, P. J. Brown, J. R. Brownstein, K. Bundy, N. G. Busca, W. Carithers, A. R. Carnero, M. A. Carr, Y. Chen, J. Comparat, N. Connolly, F. Cope, R. A. C. Croft, A. J. Cuesta, L. N. da Costa, J. R. A. Davenport, T. Delubac, R. de Putter, S. Dhital, A. Ealet, G. L. Ebelke, D. J. Eisenstein, S. Escoffier, X. Fan, N. Filiz Ak, H. Finley, A. Font-Ribera, R. Génova-Santos, J. E. Gunn, H. Guo, D. Haggard, P. B. Hall, J.-C. Hamilton, B. Harris, D. W. Harris, S. Ho, D. W. Hogg, D. Holder, K. Honscheid, J. Huehnerhoff, B. Jordan, W. P. Jordan, G. Kauffmann, E. A. Kazin, D. Kirkby, M. A. Klaene, J.-P. Kneib, J.-M. Le Goff, K.-G. Lee, D. C. Long, C. P. Loomis, B. Lundgren, R. H. Lupton, M. A. G. Maia, M. Makler, E. Malanushenko, V. Malanushenko, R. Mandelbaum, M. Manera, C. Maraston, D. Margala, K. L.

Masters, C. K. McBride, P. McDonald, I. D. McGreer, R. G. McMahon, O. Mena, J. Miralda-Escudé, A. D. Montero-Dorta, F. Montesano, D. Muna, A. D. Myers, T. Naugle, R. C. Nichol, P. Noterdaeme, S. E. Nuza, M. D. Olmstead, A. Oravetz, D. J. Oravetz, R. Owen, N. Padmanabhan, N. Palanque-Delabrouille, K. Pan, J. K. Parejko, I. Pâris, W. J. Percival, I. Pérez-Fournon, I. Pérez-Ràfols, P. Petitjean, R. Pfaffenberger, J. Pforr, M. M. Pieri, F. Prada, A. M. Price-Whelan, M. J. Raddick, R. Rebolo, J. Rich, G. T. Richards, C. M. Rockosi, N. A. Roe, A. J. Ross, N. P. Ross, G. Rossi, J. A. Rubiño-Martin, L. Samushia, A. G. Sánchez, C. Sayres, S. J. Schmidt, D. P. Schneider, C. G. Scóccola, H.-J. Seo, A. Shelden, E. Sheldon, Y. Shen, Y. Shu, A. Slosar, S. A. Smee, S. A. Snedden, F. Stauffer, O. Steele, M. A. Strauss, A. Streblyanska, N. Suzuki, M. E. C. Swanson, T. Tal, M. Tanaka, D. Thomas, J. L. Tinker, R. Tojeiro, C. A. Tremonti, M. Vargas Magaña, L. Verde, M. Viel, D. A. Wake, M. Watson, B. A. Weaver, D. H. Weinberg, B. J. Weiner, A. A. West, M. White, W. M. Wood-Vasey, C. Yeche, I. Zehavi, G.-B. Zhao, and Z. Zheng. The Baryon Oscillation Spectroscopic Survey of SDSS-III. Astronomical Journal, 145:10, January 2013.

[19] N. Palanque-Delabrouille, C. Yèche, A. Borde, J.-M. Le Goff, G. Rossi, M. Viel, É. Aubourg, S. Bailey, J. Bautista, M. Blomqvist, A. Bolton, J. S. Bolton, N. G. Busca, B. Carithers, R. A. C. Croft, K. S. Dawson, T. Delubac, A. Font-Ribera, S. Ho, D. Kirkby, K.-G. Lee, D. Margala, J. Miralda-Escudé, D. Muna, A. D. Myers, P. Noterdaeme, I. Pâris, P. Petitjean, M. M. Pieri, J. Rich, E. Rollinde, N. P. Ross, D. J. Schlegel, D. P. Schneider, A. Slosar, and D. H. Weinberg. The one-dimensional Lyα forest power spectrum from BOSS. A&A, 559:A85, November 2013.

[20] S. López, V. D'Odorico, S. L. Ellison, G. D. Becker, L. Christensen, G. Cupani, K. D. Denney, I. Pâris, G. Worseck, T. A. M. Berg, S. Cristiani, M. Dessauges-Zavadsky, M. Haehnelt, F. Hamann, J. Hennawi, V. Iršič, T.-S. Kim, P. López, R. Lund Saust, B. Ménard, S. Perrotta, J. X. Prochaska, R. Sánchez-Ramírez, M. Vestergaard, M. Viel, and L. Wisotzki. XQ-100: A legacy survey of one hundred $z = 3.5 - 4.5$ quasars observed with VLT/X-shooter. A&A, 594:A91, October 2016.

[21] D. H. Weinberg, J. S. Bullock, F. Governato, R. Kuzio de Naray, and A. H. G. Peter. Cold dark matter: Controversies on small scales. Proceedings of the National Academy of Science, 112:12249–12255, October 2015.

[22] R. Adhikari, M. Agostini, N. A. Ky, T. Araki, M. Archidiacono, M. Bahr, J. Behrens, F. Bezrukov, P. S. Bhupal Dev, D. Borah, A. Boyarsky, A. de Gouvea, C. A. d. S. Pires, H. J. de Vega, A. G. Dias, P. Di Bari, Z. Djurcic, K. Dolde, H. Dorrer, M. Durero, O. Dragoun, M. Drewes, C. E. Düllmann, K. Eberhardt, S. Eliseev, C. Enss, N. W. Evans, A. Faessler, P. Filianin, V. Fischer, A. Fleischmann, J. A. Formaggio, J. Franse, F. M. Fraenkle, C. S. Frenk, G. Fuller, L. Gastaldo, A. Garzilli, C. Giunti, F. Glück, M. C. Goodman, M. C. Gonzalez-Garcia, D. Gorbunov, J. Hamann, S. Hannestad, J. Heeck, V. Hannen, S. H. Hansen, C. Hassel, F. Hofmann, T. Houdy, A. Huber, D. Iakubovskyi, A. Ianni, A. Ibarra, R. Jacobsson, T. Jeltema, S. Kempf, T. Kieck, M. Korzeczek, V. Kornoukhov, T. Lachenmaier, M. Laine, P. Langacker, T. Lasserre, J. Lesgourgues, D. Lhuillier, Y. F. Li, W. Liao, A. W. Long, M. Maltoni, G. Mangano, N. E. Mavromatos, N. Menci, A. Merle, S. Mertens, A. Mirizzi, B. Monreal, A. Nozik, A. Neronov, V. Niro, Y. Novikov, L. Oberauer, E. Otten, N. Palanque-Delabrouille, M. Pallavicini, V. S. Pantuev, E. Papastergis, S. Parke, S. Pastor, A. Patwardhan, A. Pilaftsis, D. C. Radford, P. C.-O. Ranitzsch, O. Rest, D. J. Robinson, P. S. Rodrigues da Silva, O. Ruchayskiy, N. G. Sanchez, M. Sasaki, N. Saviano, A. Schneider, F. Schneider, T. Schwetz, S. Schönert, F. Shankar, N. Steinbrink, L. Strigari, F. Suekane, B. Suerfu, R. Takahashi, N. T. H. Van, I. Tkachev, M. Totzauer, Y. Tsai, C. G. Tully, K. Valerius, J. Valle, D. Venos, M. Viel, M. Y. Wang, C. Weinheimer, K. Wendt, L. Winslow, J. Wolf, M. Wurm, Z. Xing, S. Zhou, and K. Zuber. A White Paper on keV Sterile Neutrino Dark Matter. ArXiv e-prints, February 2016.

[23] E. Bulbul, M. Markevitch, A. Foster, E. Miller, M. Bautz, M. Loewenstein, S. W. Randall, and R. K. Smith. Searching for the 3.5 keV Line in the Stacked Suzaku Observations of Galaxy Clusters. Astrophys. J. , 831:55, November 2016.

[24] A. Boyarsky, O. Ruchayskiy, D. Iakubovskyi, and J. Franse. Unidentified Line in X-Ray Spectra of the Andromeda Galaxy and Perseus Galaxy Cluster. Physical Review Letters, 113(25):251301, December 2014.

[25] L. Hui, J. P. Ostriker, S. Tremaine, and E. Witten. On the hypothesis that cosmological dark matter is composed of ultra-light bosons. ArXiv e-prints, October 2016.

[26] P. Bode, J. P. Ostriker, and N. Turok. Halo Formation in Warm Dark Matter Models. Astrophys. J. , 556:93–107, July 2001.

[27] A. M. Brooks and A. Zolotov. Why Baryons Matter: The Kinematics of Dwarf Spheroidal Satellites. Astrophys. J. , 786:87, May 2014.

[28] A. R. Wetzel, P. F. Hopkins, J.-h. Kim, C.-A. Faucher-Giguère, D. Kereš, and E. Quataert. Reconciling Dwarf Galaxies with ΛCDM Cosmology: Simulating a Realistic Population of Satellites around a Milky Way-mass Galaxy. Astrophysical Journal Letters, 827:L23, August 2016.

[29] V. Iršič, M. Viel, T. A. M. Berg, V. D'Odorico, M. G. Haehnelt, S. Cristiani, G. Cupani, T.-S. Kim, S. Lopez, S. Ellison, G. D. Becker, L. Christensen, K. D. Denney, G. Worseck, and J. S. Bolton. The Lyman-alpha forest power spectrum from the XQ-100 Legacy Survey. MNRAS, 2017.

[30] Volker Springel. The cosmological simulation code GADGET-2. MNRAS, 364:1105–1134, 2005.

[31] J. S. Bolton, E. Puchwein, D. Sijacki, M. G. Haehnelt, T.-S. Kim, A. Meiksin, J. A. Regan, and M. Viel. The Sherwood simulation suite: overview and data comparisons with the Lyman-alpha forest at redshifts $2 < z < 5$. ArXiv e-prints, May 2016.

[32] Planck Collaboration, P. A. R. Ade, N. Aghanim, M. Arnaud, M. Ashdown, J. Aumont, C. Baccigalupi, A. J. Banday, R. B. Barreiro, J. G. Bartlett, and et al. Planck 2015 results. XIII. Cosmological parameters. A&A, 594:A13, September 2016.

[33] J. S. Bolton, M. Viel, T.-S. Kim, M. G. Haehnelt, and R. F. Carswell. Possible evidence for an inverted temperature-density relation in the intergalactic medium

from the flux distribution of the Lyα forest. MNRAS, 386:1131–1144, May 2008.

[34] G. D. Becker, J. S. Bolton, M. G. Haehnelt, and W. L. W. Sargent. Detection of extended He II reionization in the temperature evolution of the intergalactic medium. MNRAS, 410:1096–1112, January 2011.

[35] F. Nasir, J. S. Bolton, and G. D. Becker. Inferring the IGM thermal history during reionization with the Lyman α forest power spectrum at redshift z $\sim$ 5. MNRAS, 463:2335–2347, December 2016.

[36] G. Worseck, J. X. Prochaska, J. M. O'Meara, G. D. Becker, S. L. Ellison, S. Lopez, A. Meiksin, B. Ménard, M. T. Murphy, and M. Fumagalli. The Giant Gemini GMOS survey of $z_{em} > 4.4$ quasars - I. Measuring the mean free path across cosmic time. MNRAS, 445:1745–1760, December 2014.

[37] A. D'Aloisio, M. McQuinn, and H. Trac. Large Opacity Variations in the High-redshift Lyα Forest: The Signature of Relic Temperature Fluctuations from Patchy Reionization. Astrophysical Journal Letters, 813:L38, November 2015.

[38] G. D. Becker, J. S. Bolton, P. Madau, M. Pettini, E. V. Ryan-Weber, and B. P. Venemans. Evidence of patchy hydrogen reionization from an extreme Lyα trough below redshift six. MNRAS, 447:3402–3419, March 2015.

[39] P. McDonald, U. Seljak, R. Cen, P. Bode, and J. P. Ostriker. Physical effects on the Lyα forest flux power spectrum: damping wings, ionizing radiation fluctuations and galactic winds. MNRAS, 360:1471–1482, July 2005.

[40] J. Schaye, T. Theuns, M. Rauch, G. Efstathiou, and W. L. W. Sargent. The thermal history of the intergalactic medium*. MNRAS, 318:817–826, November 2000.

[41] A. Lidz, C.-A. Faucher-Giguère, A. Dall'Aglio, M. McQuinn, C. Fechner, M. Zaldarriaga, L. Hernquist, and S. Dutta. A Measurement of Small-scale Structure in the 2.2-4.2 Lyα Forest. Astrophys. J. , 718:199–230, July 2010.

[42] E. Puchwein, J. S. Bolton, M. G. Haehnelt, P. Madau, G. D. Becker, and F. Haardt. The photoheating of the intergalactic medium in synthesis models of the UV background. MNRAS, 450:4081–4097, July 2015.

[43] P. R. Upton Sanderbeck, A. D'Aloisio, and M. J. McQuinn. Models of the thermal evolution of the intergalactic medium after reionization. MNRAS, 460:1885–1897, August 2016.

[44] A. Garzilli, A. Boyarsky, and O. Ruchayskiy. Cutoff in the Lyman {\alpha} forest power spectrum: warm IGM or warm dark matter? ArXiv e-prints, October 2015.

[45] J. Oñorbe, J. F Hennawi, and Z. Lukić. Self-Consistent Modeling of Reionization in Cosmological Hydrodynamical Simulations. ArXiv e-prints, July 2016.

[46] K. Lai, A. Lidz, L. Hernquist, and M. Zaldarriaga. The Impact of Temperature Fluctuations on the Lyα Forest Power Spectrum. Astrophys. J. , 644:61–70, June 2006.

[47] Nickolay Y. Gnedin and Lam Hui. Probing the universe with the Lyman alpha forest: 1. Hydrodynamics of the low density IGM. Mon. Not. Roy. Astron. Soc., 296:44–55, 1998.

[48] M. McQuinn, A. Lidz, M. Zaldarriaga, L. Hernquist, P. F. Hopkins, S. Dutta, and C.-A. Faucher-Giguère. He II Reionization and its Effect on the Intergalactic Medium. Astrophys. J. , 694:842–866, April 2009.